nature astronomy

Article

https://doi.org/10.1038/s41550-022-01825-6

Astrophysical constraints from the SARAS 3 non-detection of the cosmic dawn sky-averaged 21-cm signal

Received: 10 May 2022

Accepted: 21 September 2022

Published online: 28 November 2022

Check for updates

H. T. J. Bevins[1,2] ✉, A. Fialkov[2,3], E. de Lera Acedo[1,2], W. J. Handley[1,2], S. Singh[4], R. Subrahmanyan[5] & R. Barkana[6,7,8]

Observations of the redshifted 21-cm line of atomic hydrogen have provided several upper limits on the 21-cm power spectrum and a tentative detection of the sky-averaged signal at redshift $z \approx 17$. Made with the Experiment to Detect the Global EoR Signature (EDGES) low-band antenna, this claim was recently disputed by the SARAS 3 experiment, which reported a non-detection and is the only available upper limit strong enough to constrain cosmic dawn astrophysics. We use these data to constrain a population of radio-luminous galaxies ~200 million years after the Big Bang ($z \approx 20$). We find, using Bayesian data analysis, that the data disfavour (at 68% confidence) radio-luminous galaxies in dark-matter haloes with masses of $4.4 \times 10^5\, M_\odot \lesssim M \lesssim 1.1 \times 10^7\, M_\odot$ (where $M_\odot$ is the mass of the Sun) at $z = 20$ and galaxies in which >5% of the gas is converted into stars. The data disfavour galaxies with a radio luminosity per star formation rate of $L_r/\mathrm{SFR} \gtrsim 1.549 \times 10^{25}\ \mathrm{W\ Hz^{-1}}\, M_\odot^{-1}\ \mathrm{yr}$ at 150 MHz, around 1,000 times brighter than today, and, separately, a synchrotron radio background in excess of the cosmic microwave background by ≥6% at 1.42 GHz.

Understanding the early Universe, when the first stars and galaxies formed, is one of the major science goals of a number of new observatories. The recently launched James Webb Space Telescope (JWST) will directly image these early galaxies in deep near-infrared surveys. Its increased sensitivity in comparison with the previous generation of telescopes will allow JWST to target faint, high-redshift galaxies existing during the first few hundred million years of cosmic history all the way out to the cosmological redshift of $z \approx 20$ (ref. [1]). Future confirmed and proposed X-ray missions, such as the Advanced Telescope for High-Energy Astrophysics[2], the Lynx X-ray Observatory[3] and the Advanced X-ray Imaging Satellite[4], will supplement this exploration by observing the hot gas in the Universe. Radio telescopes aim to complement this picture by mapping the neutral intergalactic gas across the first billion years of cosmic history via observations of the 21-cm spin-flip transition of atomic hydrogen seen against the radio background radiation, which is usually assumed to be the cosmic microwave background (CMB)[5,6].

Upper limits on the 21-cm signal from the epoch of reionization (EoR, $z \approx 6$–15) measured by both radiometers[7,8], which probe the sky-averaged (global) 21-cm signal and large interferometric arrays[9–13] that target fluctuations, are already available. These data have recently allowed constraints to be derived on the astrophysical processes at the EoR[14–21] and are in a broad agreement with other probes of reionization history such as high-redshift quasars and galaxies[22–26].

The observational status of the cosmic dawn signal originating from higher redshifts ($z \approx 15$–30) is more intriguing: the EDGES Low-Band collaboration reported a tentative detection of an absorption profile at $z \approx 17$ (ref. [27]), which is at least two times deeper than is

[1]Astrophysics Group, Cavendish Laboratory, Cambridge, UK. [2]Kavli Institute for Cosmology, Cambridge, UK. [3]Institute of Astronomy, University of Cambridge, Cambridge, UK. [4]Raman Research Institute, Bangalore, India. [5]Space & Astronomy CSIRO, Kensington, Western Australia, Australia. [6]School of Physics and Astronomy, Tel-Aviv University, Tel-Aviv, Israel. [7]Institute for Advanced Study, Princeton, NJ, USA. [8]Department of Astronomy and Astrophysics, University of California, Santa Cruz, CA, USA. ✉e-mail: htjb2@cam.ac.uk

predicted by conventional theoretical modelling[28,29]. Such a strong signal implies either the existence of an excess radio background above the CMB[27,30] or a non-standard thermal history of the intergalactic gas[27,31]. The cosmological origin of this signal was recently disputed by the SARAS 3 collaboration, who conducted an independent experiment and reported a non-detection of the EDGES best-fit profile in their data[32–35]. It has also been shown that the reported EDGES signal can partially be explained by invoking sinusoidal instrument systematics[36–39]; however, additional efforts are being made to verify the EDGES detection and to make independent measurements of the 21-cm signal from cosmic dawn both with interferometers[20,40–42] and radiometers (http://www.physics.mcgill.ca/mist/)[11,43].

The non-detection by SARAS 3 of the EDGES profile increases the likelihood of the anomalous absorption feature being non-cosmological and brings the focus back to the more conventional astrophysical scenarios. In this work we use the SARAS 3 data to provide constraints on the astrophysical processes at cosmic dawn. We consider a potential population of high-redshift radio-luminous galaxies that contribute to the radio background radiation, thus affecting the 21-cm signal. In general, radio galaxies are expected in standard astrophysical scenarios[44,45], and it is only for extremely high radio luminosity values that their contribution is large enough to explain the EDGES signal[27,30,44–48]. Here we consider a wide selection of models that vary astrophysical properties of high-redshift galaxies over a broad range. We repeat our analysis for two additional scenarios (shown in Supplementary Information): one with the CMB as the radio background radiation[29] and the other with a phenomenological synchrotron radio background in addition to the CMB[48].

In the 'Data' section we discuss the SARAS 3 data in more detail. The 'Cosmological 21-cm signal' section introduces the different modelled components in our analysis and discusses how we determined constraints on the astrophysical processes at cosmic dawn, with further details given in Methods. Our constraints on high-redshift radio galaxies are discussed in the Results. Additional astrophysical models are discussed in Supplementary Information.

Data

SARAS 3 is a radiometer based on a monocone antenna that has made observations of the sky from a location in Southern India in the 43.75–87.5 MHz band, targeting the cosmological 21-cm signal from $z \approx 15$–32 (refs. [32–34]). The experiment is the first global 21-cm experiment of its kind to take observations while floating on a body of water, which is expected to improve the total efficiency of the antenna. The total efficiency quantifies how the sky radiation is coupled to the antenna, including losses in the local environment of the antenna (such as ground or water beneath the antenna[33]), and prevents non-smooth systematics caused by stratified ground emission that can impede the detection of a global signal from being introduced[21].

Fifteen hours of observations were integrated in the frequency range 55–85 MHz ($z \approx 15$–25), reduced after radio frequency interference filtering, with corrections made for emission from the water beneath the antenna and receiver noise temperature. The data were then appropriately scaled, given an estimate of the total efficiency, to produce an average measurement of the sky temperature, $T_{\rm sky}$, which we expected to be the sum of the Galactic and extra-Galactic foregrounds, $T_{\rm fg}$, and the cosmological 21-cm signal, T_{21}.

A log–log polynomial foreground model was previously fitted to the data in combination with the phenomenological best-fit EDGES absorption profile multiplied by a scale factor, s, using a Markov Chain Monte Carlo analysis. The data were shown to reject the presence of the EDGES signal with 95.3% confidence, and a series of EDGES-like signals, representing the likelihood distributions of uncertainties in the profile parameters, were rejected with a significance of 90.4% (ref. [35]). The SARAS 3 measurement of the sky-averaged radio spectrum thus represents a non-detection of the EDGES absorption feature, with the potential to constrain astrophysical scenarios that result in signals larger in magnitude than the instrument noise.

Table 1 | The neural network emulation

	Radio background		
	Radio galaxies	Synchrotron	CMB only
Number of training models	4,311	9,304	5,137
Number of testing models	479	1,034	570
Mean r.m.s.e (mK)	5.11	7.98	0.78
95 percentile r.m.s.e. (mK)	20.53	23.06	2.67
Worst r.m.s.e. (mK)	81.70	85.65	13.36

The table summarizes the number of models used to train and test the three different neural network emulators used in this paper, along with summary statistics for their accuracies. r.m.s.e., root mean squared error.

Cosmological 21-cm signal

To provide constraints on the astrophysical processes at cosmic dawn using the SARAS 3 data, we needed to model the global 21-cm signal. Theoretical predictions of the signal are made difficult owing to the non-local impact of the non-uniform radiative fields produced by a distribution of luminous sources. Either numerical or semi-numerical methods are required to calculate the three-dimensional (3D) 21-cm signal and evolve it with time. The global signal can then be calculated as the spatial average, although 1D radiative transfer codes are also used to calculate the global signal[49]. As astrophysical processes at high redshifts are poorly understood, a range of theoretical predictions for the 21-cm signal need to be computed for different astrophysical scenarios, which can then be constrained by data. In this work we used a semi-numerical method[29,50–53] to calculate the 21-cm signal from an evolving simulated Universe. The calculation takes into account important processes that shape the 21-cm signal: the baryonic matter in the early Universe is predominantly composed of atomic hydrogen and, as the first stars and black holes form at $z \approx 30$ (refs. [54,55]), they affect both the total intensity and the fluctuations of the hydrogen signal. Radiation from the first stars in the Lyman band plays a fundamental role as it enables observations of the 21-cm signal against the radio background by coupling the characteristic temperature of the spin-flip transition, the spin temperature $T_{\rm S}$, to the kinetic temperature of the gas, $T_{\rm K}$ (refs. [56,57]). At cosmic dawn, radiation is typically warmer than the gas, and the signal appears as an absorption feature against the radio background. Heating of the intergalactic medium subsequently raises the gas temperature to (and perhaps above) the radio background[29,52,53], resulting in emission at low redshift. This evolution culminates at the EoR when ultraviolet radiation from stars ionizes the neutral hydrogen in the intergalactic medium and the signal disappears. If it exists at high redshift, any additional radio background above the CMB would contribute to the 21-cm signal by increasing the temperature of the radio background, $T_{\rm rad}$, and thus deepening the absorption profile[30,44–46,48].

For a specified set of astrophysical parameters, each simulation can take a few hours to produce the desired global 21-cm signal. However, to derive parameter constraints from real data, a multitude of such signals needs to be created to probe the vast astrophysical parameter space. The application of machine learning to the problem of signal modelling is common in the analysis of data from 21-cm experiments[16,17,20,21] and allows different physical signal models to be generated quickly using computationally intensive fitting algorithms. Starting from a set of the simulated signals, we used neural networks[58] to interpolate the astrophysical parameter space (see Methods and Table 1 for a discussion of the network training and accuracy).

https://doi.org/10.1038/s41550-022-01825-6

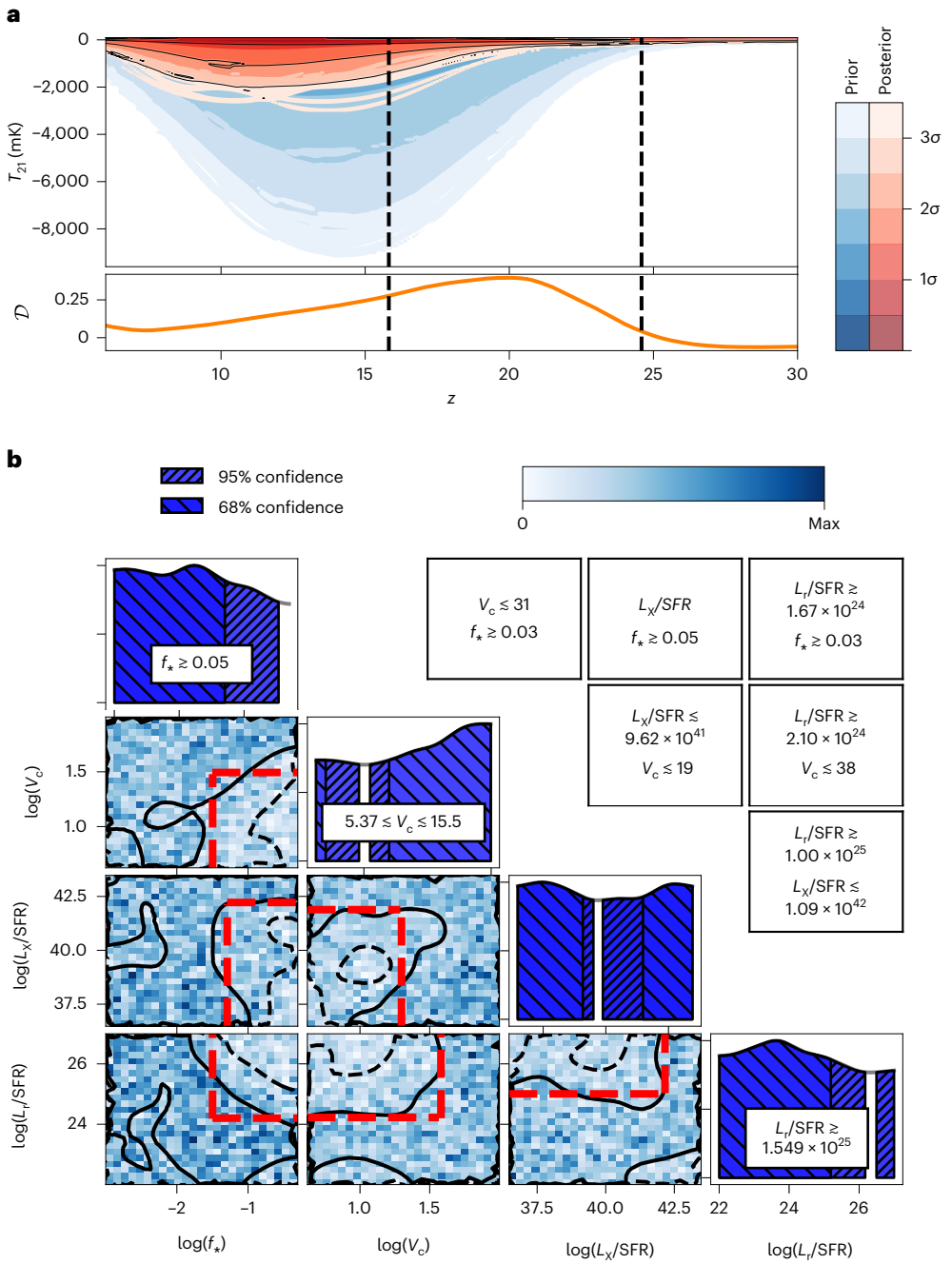

Fig. 1 | SARAS 3 constraints on high-redshift radio galaxies. a, Top: the data disfavour deep global signals, as can be seen by comparing the functional prior with the posterior. Bottom: the Kullback–Leibler divergence, $\mathcal{D}$, as a function of redshift between the functional prior and posterior. $\mathcal{D}$ gives a measure of the information gain when moving from one to the other and illustrates the constraining power of the SARAS 3 data, which peaks at around $z \approx 20$. The dashed vertical lines mark the SARAS 3 band. **b**, The corresponding 1D and 2D posteriors for the astrophysical parameters found when fitting the foreground and a global 21-cm signal. V_c is in km s^{-1}, L_r/SFR is in W Hz^{-1} $M_\odot^{-1}$ yr calculated at 150 MHz and the X-ray luminosity per unit SFR, L_X/SFR, is in erg s^{-1} $M_\odot^{-1}$ yr. The corresponding 1D posterior with marked 68% disfavoured regions is shown in the top of each column. The colour of the 2D posteriors (colour bar) reflects the magnitude of the 2D posterior probabilities. The dashed black lines encapsulate the 95% confidence regions. The solid black lines show the 68% confidence regions for which we made a conservative approximation with the dashed red lines (to guide the eye) with the corresponding numerical values summarized in the inverted triangle table on the right. Figure produced with ANESTHETIC[76] and FGIVENX[77].

To extract constraints on the global signal, we also needed to model the foreground in the data. We did this using the same log–log polynomial as in the previous analysis of the SARAS 3 data[35] for consistency (Methods).

The theoretical cosmic dawn 21-cm signal is sensitive to the process of star formation, the thermal history and the temperature of the radio background radiation (Methods). The root mean squared (r.m.s.) of the appropriately weighted SARAS 3 residuals after foreground modelling and removal is 213 mK at their native spectrum resolution of 61 kHz (ref. [35]). Signals that are within the sensitivity of the instrument and would have been detected are those with deeper absorption troughs that have strong variation within the band. Such signals are typically created in scenarios with high intensity of the Lyα photons, corresponding to a combination of low minimum virial

https://doi.org/10.1038/s41550-022-01825-6

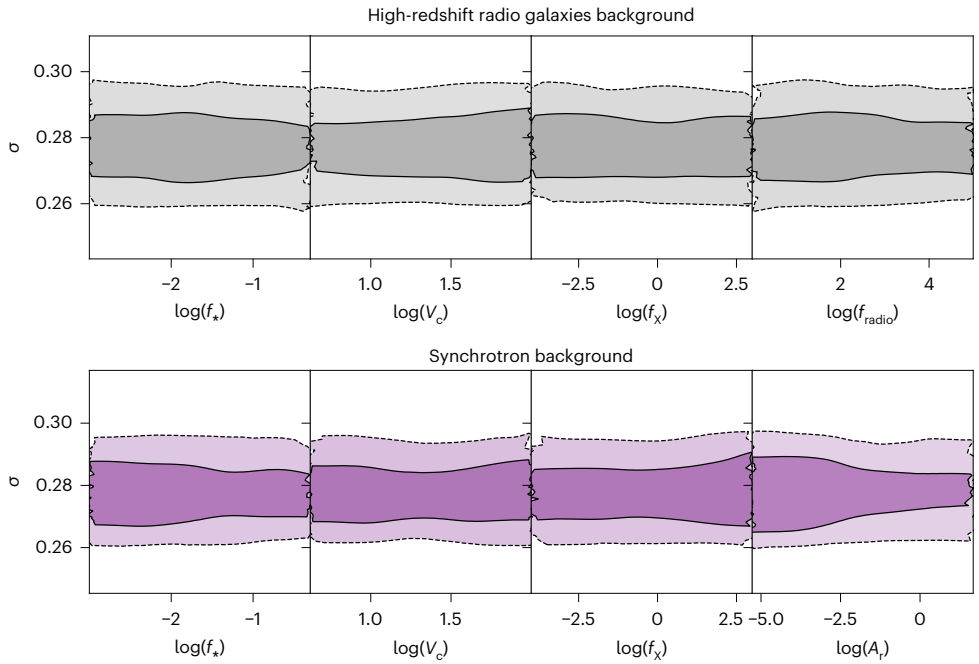

Fig. 2 | The relationship between the astrophysical parameters and the noise. The standard deviation, σ, of the assumed Gaussian noise is uncorrelated with the astrophysical parameters in both models fit with an excess radio background from high-redshift radio galaxies (top) and fit with an excess from a homogeneous synchrotron source (bottom), and consequently we would expect that a full treatment of any frequency dependence of the noise in the data, which is left for future work, will have little impact on the derived parameter constraints. The darker shaded regions and solid lines indicate 68% confidence regions, and the lighter shaded regions and dashed lines indicate 95% confidence regions. f_* is the star formation efficiency, V_c is the virial circular velocity, f_X is the X-ray production efficiency, f_{radio} is the radio production efficiency in the radio galaxies and A_r is the fractional increase in the radio background from the homogeneous synchrotron source.

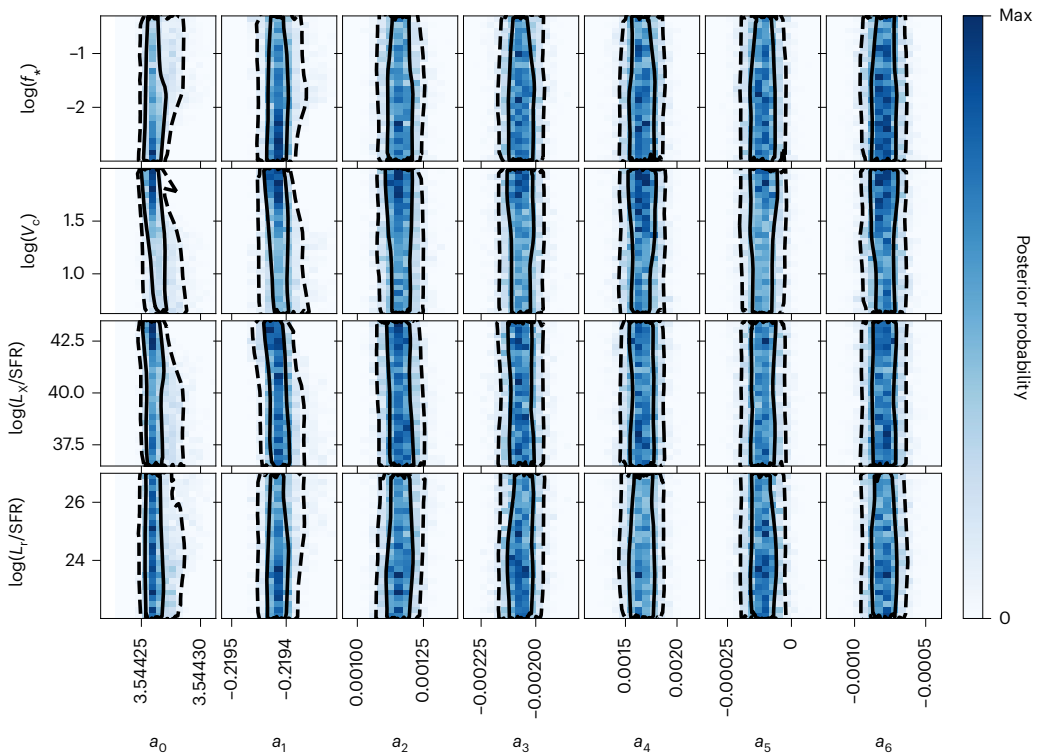

Fig. 3 | The relationship between the foreground and astrophysical parameters. The 2D posterior distributions between the astrophysical parameters and coefficients of the foreground model, a_0–a_6, found when fitting the data with the radio galaxy radio background models. We see no clear correlations between the two sets of parameters, indicating that they are independent of each other. The dashed and solid lines show 95% and 68% confidence regions, respectively.

https://doi.org/10.1038/s41550-022-01825-6

Table 2 | The astrophysical priors

Parameter	Radio background	Range
f_*	CMB only, synchrotron, radio galaxies	0.001–0.5
V_c (km s^{-1})	CMB only, synchrotron, radio galaxies	4.2–100
f_X	CMB only, synchrotron, radio galaxies	0.001–1,000
f_{radio}	Radio galaxies	1.0–99,500
$A_r^{1,420}$	Synchrotron	0–47
τ	CMB only	0.026–0.103
	Synchrotron	0.016–0.158
	Radio galaxies	0.035–0.077
α	CMB only	1.0–1.5
E_{min} (keV)	CMB only	0.1–3.0
R_{mfp} (Mpc)	CMB only, synchrotron, radio galaxies	Fixed at 30, 40 and 40

The prior ranges were designed to encompass the current uncertainty in the properties of the high-redshift Universe. The emulators were unreliable outside these bounds. Note that τ is not an important parameter in the SARAS 3 band, but we trained the models with this parameter as an input, performed fits with it and then marginalized over it. Similarly, R_{mfp} is only important at lower redshifts outside the SARAS 3 band. The global signal has only a weak dependence on this parameter, and so we fixed its value of 40 Mpc for the radio galaxies and radio synchrotron backgrounds, while in the CMB-only case, it was fixed to 30 Mpc. E_{min} is the low energy cutoff of the X-ray spectral energy density, and $A_r^{1,420}$ is the fractional increase in the radio background temperature above the CMB at 1,420 MHz from the homogeneous synchrotron source.

circular velocities V_c and high star formation efficiencies f_*, and a strong contrast between the gas temperature and the temperature of the radio background (that is, for low values of the X-ray production efficiency f_X and high radio production efficiencies f_{radio}). We therefore expected the SARAS 3 data to constrain these model parameters. In our analysis, we marginalized parameters, including the CMB optical depth, τ, and the mean free path of ionizing photons, R_{mfp}, that determined the structure of the signal during the EoR because they were not relevant to the SARAS 3 band.

We used the Bayesian nested sampling algorithm to perform our model fitting[59] (Methods).

Results

In this section, we discuss the SARAS 3 constraints in the redshift range $z \approx 15$–25 on a population of high-redshift radio-luminous galaxies and show the main results in Fig. 1. Constraints on models with the CMB-only background and an excess radio background from a phenomenological synchrotron source[48] are discussed in Supplementary Information.

We calculated the posterior distribution (using equation (1)), which is a multivariate probability distribution for the 13 parameters that describe the foreground (7 polynomial coefficients), noise (1 parameter, the standard deviation of the Gaussian noise in the data; Methods) and the cosmological 21-cm signal (5 astrophysical parameters: f_{radio}, f_*, V_c, f_X and τ). We then marginalized over the foreground parameters, noise and τ, which allowed us to calculate the likelihood of different astrophysical 21-cm signals. The standard deviation of the noise was shown to be independent of the astrophysical parameters in Fig. 2 for excess background models. We subsequently derived limits on the parameters related to star formation, heating and the excess radio background above the CMB. We discuss the foreground model[35] in more detail in Methods and Supplementary Information. We note here that in fits with both a foreground and 21-cm signal model we found no correlation between the two sets of parameters, as can be seen in Fig. 3.

We found no evidence for an astrophysical signal in the data. The foreground-only fit consistently had a larger log-evidence by approximately 10 log units when compared with fits with signal profiles (that is, $\mathcal{Z}_{\mathbf{M}_1} > \mathcal{Z}_{\mathbf{M}_2}$ as described in Methods). Therefore, any cosmological signal present in the data is likely to be undetectable in the residuals (with r.m.s. of ~213 mK), after foreground modelling and subtraction. As the predicted amplitude of the 21-cm signal is expected to be lower than ~165 mK (ref. [29]) in the case of the standard scenario with the CMB as the only source of the background radiation, the SARAS 3 constraints on this scenario are very weak (Supplementary Information). However, in the case of an excess radio background, the predicted signals can be much stronger, allowing us to disfavour regions of the astrophysical parameter space.

Figure 1a shows the contraction from the initial set of possible 21-cm signals (prior (blue region); details of the astrophysical priors can be found in Methods and Table 2) to the set of scenarios that are allowed by the data (that is, the functional posterior (red)). The functional posterior and prior were produced by taking the posterior samples returned from our nested sampling run and a representative set of prior samples and transforming them into realizations of the global 21-cm signal using the trained neural networks. Figure 1 illustrates that, as anticipated, the deepest signals and the signals with the strongest variation in the SARAS 3 band ($z = 15$–25) were disfavoured. Signals with a modest variation within the band and signals with minima at $z \lesssim 15$ were indistinguishable from the foregrounds and thus cannot be ruled out.

We could estimate the quantitative contribution of the SARAS 3 measurement to our understanding of the high-redshift Universe by calculating the information gain using the value of $\mathcal{D}$ (ref [60]) between the functional prior and posterior (bottom of Fig. 1a). By definition, $\mathcal{D}$ has arbitrary scaling but should always be ≥ 0. We found that $\mathcal{D}$ was highest, meaning that the information gain was largest, at $z \approx 20$, which corresponds to the middle of the SARAS 3 band. Owing to the dependence of the 21-cm signal on the star formation and heating histories, we saw that the constraining power of the SARAS 3 measurement extended to lower redshifts outside the SARAS 3 frequency band ($\mathcal{D}$ is non-vanishing). On the other hand, $\mathcal{D}$ was approximately zero at $z \gtrsim 30$, where the global 21-cm signals are dominated by cosmology, rather than by astrophysics.

We next considered the astrophysical parameter constraints and show the corresponding 1D and 2D posteriors in Fig. 1b. The visualization of the constraints on the signal parameters is non-trivial and is achieved in 2D and 1D via marginalization. Marginalization involves integrating the dependence on the $N-1$ or $N-2$ parameters out of the posterior distribution to leave 1D and 2D distributions for the astrophysical parameters. Key numerical results and comparison with SARAS 2[21] and HERA[20] constraints are summarized in Table 3. To guide the eye, we show the approximate 2D constraints (red dashed lines) roughly corresponding to the 68% confidence contours (solid black lines) and list these limits in Fig. 1b (inverted triangle table). Note that there are regions of low probability outside these guides. From Fig. 1 it is clear that SARAS 3 data most strongly constrain the process of primordial star formation (clear trends in the 1D posterior probabilities of V_c and f_*) and the strength of the radio background (limits on the radio luminosity per star formation rate at 150 MHz, L_r/SFR) with weaker sensitivity to the heating process. However, this heating process is clearly constrained in combination with the strong radio background.

From the 1D posterior distribution, we see that the data constrain the radio production efficiency of the early sources, with the values of $L_r/\mathrm{SFR} \gtrsim 1.549 \times 10^{25}$ W Hz^{-1} $M_\odot^{-1}$ yr at 150 MHz ($f_{radio} \gtrsim 1{,}549$) being disfavoured at 68% confidence. Moreover, we expect a significant correlation between the impact of the radio background and that of the thermal history on the global 21-cm signal, as both a strong radio emission and weak X-ray heating contribute in the same direction, deepening the absorption trough. Considering the 2D posterior

https://doi.org/10.1038/s41550-022-01825-6

Table 3 | Summary of key constraints from SARAS 3 (this work), HERA and SARAS 2 experiments

	SARAS 3	HERA	SARAS 2
Signal type	Global	Power spectrum	Global
Redshift range	$z \approx 15$–25	$z \approx 8$ and $z \approx 10$	$z \approx 7$–12
L_r/SFR (W Hz^{-1} $M_\odot^{-1}$ yr)	$\gtrsim 1.549\times10^{25}$	$\gtrsim 4.00\times10^{24}$	–
L_r/SFR ∩ L_X/SFR (erg s^{-1} $M_\odot^{-1}$ yr)	$\gtrsim 1\times10^{25} \cap \lesssim 1.09\times10^{42}$	$\gtrsim 4.00\times10^{24} \cap \lesssim 7.60\times10^{39}$	$\gtrsim 4.07\times10^{24} \cap \lesssim 6.3\times10^{39}$
M ($M_\odot$)	$4.4\times10^5 \lesssim M \lesssim 1.1\times10^7$	–	–
f_*	$\gtrsim 0.05$	–	–
$f_* \cap M$ ($M_\odot$)	$\gtrsim 0.03 \cap \lesssim 8.53\times10^8$	–	–

We specify the signal type measured by each instrument (either global signal or power spectrum); redshift range targeted by each experiment; constraints on the value of L_r/SFR expressed in units of W Hz^{-1}$M_\odot^{-1}$ yr at 150 MHz; limits on L_r/SFR in combination with L_X/SFR (calculated between 0.2 and 95keV and expressed in units of erg s^{-1}$M_\odot^{-1}$ yr); limits on the mass of star forming halos, M, given in solar masses at $z = 20$, star formation efficiency f_* and, finally, constraint on f_* in combination with the halo mass. Limits on the individual parameters correspond to the regions that are disfavoured (with 68% confidence) in the 1D posteriors, and combined constraints approximately correspond to the 68% confidence limits in the 2D posteriors. Note that SARAS 2 is unable to constrain individual parameters; HERA targets the power spectrum, whereas the two SARAS experiments attempt to measure the sky-averaged signal. SARAS 3 is at much higher redshifts than the other two experiments. Although HERA provides individual constraints on L_r/SFR and L_X/SFR, here we only quote the individual constraint on L_r/SFR and the combined constraint with L_X/SFR to ease the comparison with SARAS 3 and SARAS 2. HERA data are from ref. [20] and SARAS 2 data from ref. [21].

probability in the plane L_r/SFR–L_X/SFR and the corresponding approximate contours in red, we see that high-redshift galaxies that are both efficient at producing radio photons with L_r/SFR $\gtrsim 1.00 \times 10^{25}$ W Hz^{-1} $M_\odot^{-1}$ yr and inefficient at producing X-ray photons with L_X/SFR $\lesssim 1.09 \times 10^{42}$ erg s^{-1} $M_\odot^{-1}$ yr are disfavoured. L_r/SFR and L_X/SFR are proportional to $f_{\rm radio}$ and f_X respectively, and defined in Methods.

The data disfavour (at 68% confidence) models with early onset of efficient star formation, which is characterized by low values of $5.37 \lesssim V_c \lesssim 15.5$ km s^{-1} (note that the lower limit of the prior range is $V_c = 4.2$ km s^{-1}), corresponding to small typical dark-matter haloes of $4.4 \times 10^5\ M_\odot \lesssim M \lesssim 1.1 \times 10^7\ M_\odot$ at $z = 20$ (for example, ref. [45]), and high values of $f_* \gtrsim 0.05$, interpreted as a large fraction of collapsed gas that turns into stars. Each of these criteria individually, as well as their combination, would guarantee efficient Lyα coupling, resulting in a deep high-redshift absorption profile. Considering the 2D posterior distribution, we found, using the approximate red contours on Fig. 1, that $f_* \gtrsim 0.03$ together with galaxies hosted in dark-matter haloes of masses $M \lesssim 8.53 \times 10^8\ M_\odot$ at $z = 20$ ($V_c \lesssim 31$ km s^{-1}) are disfavoured. We also found that combinations of high f_* (and low V_c) with both low X-ray efficiency and high radio efficiency are disfavoured. We note that when fitting the data with the phenomenological synchrotron radio background model, similar combinations of V_c and f_* were disfavoured (see Supplementary Information).

The derived constraints can be compared with the recently published constraints from SARAS 2[21] (Table 3 and Supplementary Fig. 2). SARAS 2 probes a lower redshift range, $z = 7$–12, and thus is complementary to SARAS 3, being more sensitive to the process of heating and ionization. However, the experiment has a comparatively low signal-to-noise ratio, meaning that any constraints derived from it are likely to be weaker. For example, one particular signal may have a magnitude lower than the SARAS 3 noise floor but higher than the SARAS 2 noise floor. This means that if that particular signal was real, SARAS 3 would have detected it but SARAS 2 would not, and hence, given the non-detection in the SARAS 3 data, the corresponding combination of astrophysical parameters will produce a lower posterior probability for SARAS 3, $\mathcal{P}(\theta|\mathbf{D}_{\rm SARAS3}, \mathbf{M}_{\rm SARAS3})$ (where $\boldsymbol{\theta}$ is the vector of the parameters of model $\mathbf{M}$ and $\mathbf{D}$ is the data), than SARAS 2, $\mathcal{P}(\theta|\mathbf{D}_{\rm SARAS2}, \mathbf{M}_{\rm SARAS2})$ (see Methods for a discussion on the posterior probability). Previously, it was found that SARAS 2 data disfavour (at approximately 68% confidence) early galaxies with L_X/SFR $\lesssim 6.3 \times 10^{39}$ erg s^{-1} $M_\odot^{-1}$ yr in combination with L_r/SFR $\gtrsim 4.07 \times 10^{24}$ W Hz^{-1} $M_\odot^{-1}$ yr (ref. [21]). This corresponds to disfavouring ~23% of the available parameter space in the L_X–L_r plane at approximately 68% confidence compared with ~32% for SARAS 3, although we note that both experiments disfavour slightly different regions of the parameter space.

The same set of astrophysical models used here has recently been constrained with an upper limit on the 21-cm power spectrum measured by HERA[20]. HERA disfavours at 68% confidence level values of L_r/SFR $\gtrsim 4 \times 10^{24}$ W Hz^{-1} $M_\odot^{-1}$ yr, as well as L_X/SFR $\lesssim 7.6 \times 10^{39}$ erg s^{-1} $M_\odot^{-1}$ yr. We found that SARAS 3 provides a similar constraint in the plane L_r/SFR and L_X/SFR, with a weaker limit on L_r/SFR but a stronger limit on L_X/SFR than HERA. Similarly, SARAS 2 gives a comparable constraint in the L_r/SFR–L_X/SFR plane. We note that both SARAS 2 and HERA probe the 21-cm signal at much lower redshifts than SARAS 3, and thus the experiments potentially probe different populations of sources. Moreover, HERA constraints come from the limit on the 21-cm power spectrum, rather than the global signal. Constraints on the 21-cm power spectrum are also available from the MWA[12,18] and LOFAR[13,17,19] interferometers. However, these limits are slightly weaker than those from HERA.

In the context of verifying the EDGES Low-Band detection, we assessed the constraining power of the SARAS 3 data on physical models that could, in principle, describe the reported absorption feature. However, we note that none of our models could fit the flattened EDGES absorption signal well. We defined EDGES-like signals using a conditional equation that ensured that the models had approximately the same central frequency, width and depth as the EDGES absorption feature but did not strictly enforce the flattened Gaussian shape of the EDGES profile[29,48]. In our analysis so far, the broad prior range was determined by our poor understanding of the high-redshift Universe. We then used the restricted EDGES-like space as our prior, as shown in Supplementary Fig. 6. We performed the fitting procedure and penalized models that did not meet the EDGES-like criteria by setting the likelihood to zero. The volume contraction from prior to posterior gave a quantitative measure of the level of consistency between the EDGES-like prior and the SARAS 3 data and could be estimated using a marginal KL divergence, $\mathcal{D}$ (ref. [60]). This effectively allowed us to say that if EDGES is true and indicative of a physical scenario, then a given percentage of the physical EDGES-like parameters space was inconsistent or ruled out by the SARAS 3 data. We found that the volume of the EDGES-like posterior, when fitting with the radio galaxy models, was 60% of the EDGES-like prior volume. In other words, 60% of the physical EDGES-like parameter space was consistent with the SARAS 3 data. See Methods and Supplementary Information for details.

Finally, we found that the data provided interesting limits on the amplitude of the synchrotron radio background in excess of the CMB, disfavouring contributions of ≥6% at a reference frequency of 1.42 GHz with 68% confidence. The constraints from SARAS 3 can be compared with the excess backgrounds inferred from ARCADE2[61] and LWA[62] experiments, assuming that the excess is cosmological and is not due to incorrect calibration of the Galactic foregrounds[63]. We found that

the 68% confidence limit on T_{rad} is significantly lower than the reported deductions from the two experiments (Supplementary Information).

Conclusion

We provide astrophysical constraints on the Universe at $z \approx 20$, corresponding to ~200 Myr after the Big Bang, using upper limits on the sky-averaged 21-cm signal measured by the SARAS 3 radiometer in the frequency range 55–85 MHz ($z \approx 15$–25). The existing constraining data (from EDGES) revealed a controversial flattened absorption profile, which awaits verification by an independent experiment. The residuals observed in SARAS 3 data, after modelling for foregrounds, do not provide evidence for a detected 21-cm signal, including the EDGES profile, and allow constraints on astrophysics at cosmic dawn to be derived.

We fitted the data with a log–log polynomial foreground model, as in the original SARAS 3 data analysis paper, together with astrophysically motivated models for the global 21-cm signal, and showed that deep global signals are disfavoured by the data. These constraints were then mapped into the astrophysical parameter space using a fully Bayesian analysis. We found that the SARAS 3 data provide constraints on the processes that are linked to the formation of first stars and galaxies, the production of radio photons at high redshifts and heating of the intergalactic medium. Our analyses disfavour, at 68% confidence, a population of radio galaxies with luminosities $L_r/\mathrm{SFR} \gtrsim 1.549 \times 10^{25}$ W Hz^{-1} $M_\odot$ yr at 150 MHz, which is a factor of 1,000 brighter than their low-redshift counterparts, and a synchrotron radio background in excess of the CMB of ≥6% at 1.42 GHz. We also found correlation between the constraints on the radio background and on the thermal history of the global 21-cm signal, showing that galaxies that are both luminous in the radio band and inefficient at producing X-ray photons are disfavoured. Finally, the non-detection of the 21-cm signal in the SARAS 3 data could be used to derive constraints on the properties of the first star-forming regions. We found that, as an approximation to the 68% confidence constraint, the data disfavoured efficient star formation at high redshifts with a minimum mass of star-forming haloes of $M \lesssim 8.53 \times 10^8\ M_\odot$ at $z = 20$ in which ≥3% of the gas is converted into stars.

Lessons learned about the astrophysics of the infant Universe from the SARAS 3 analysis can be contrasted with those from other instruments, specifically with the EDGES low-band detection at $z \approx 17$, as well as the astrophysical limits derived from the SARAS 2 data at $z \approx 7$–12 and the limits from HERA on the 21-cm power spectrum at $z \approx 8$–10, MWA at $z \approx 6.7$–8.5 (refs. [12,18]) and LOFAR at $z \approx 9$ (refs. [13,19]). For example, by conditioning the prior parameter space to be compatible with the EDGES detection and neglecting the steep walls of the feature, we found that ~60% of the available parameter space was still consistent with the SARAS 3 data.

Although the SARAS 3 constraints on the high-redshift astrophysical processes are weak, the analysis presented here demonstrates the potential of the 21-cm line as a probe for the early Universe. The cosmic dawn constraints are expected to tighten in the next few years as new low-frequency 21-cm experiments will be coming online[41,64,65].

Methods

Nested sampling

To identify constraints on the parameter space of the global signal, we used the nested sampling[59] algorithm implemented with POLYCHORD[66,67]. Samples of the parameter space of model **M** were derived using Bayes theorem

$$P(\theta|\mathbf{D},\mathbf{M}) = \frac{\mathcal{L}(\theta)\pi(\theta)}{\mathcal{Z}}, \quad (1)$$

where $\mathcal{L}$ is the likelihood representing the probability that we observe the data given the model, π is the prior probability representing our knowledge of the parameter space before we performed any fitting, and $\mathcal{Z}$ is the evidence that normalizes the posterior, $P(\boldsymbol{\theta}|\mathbf{D},\mathbf{M})$. Nested sampling generates samples from the likelihood and prior probabilities to numerically approximate $\mathcal{Z}$ and effectively sample the posterior. A higher value of $\mathcal{Z}$ when fitting model **M**1 to the data in comparison to when fitting model $\mathbf{M}_2$ indicates a preference for the former. This means that the evidence can be used to determine whether a signal is present in the data. For example, if $\mathbf{M}_1$ comprises just a foreground model and $\mathbf{M}_2$ includes both a foreground and signal model, then $\mathcal{Z}_{\mathbf{M}_1} > \mathcal{Z}_{\mathbf{M}_2}$ means that we do not require a signal model to effectively describe the data.

The posterior distribution could then be interpreted as constraints on the model. The use of Bayesian inference is becoming more common in global 21-cm analysis and is an effective method to constrain the astrophysical processes in the early Universe[21,64,65]. Throughout our analysis, we assumed a Gaussian likelihood function, $\mathcal{L}$, and a Gaussian noise distribution with a constant standard deviation, σ

$$\log \mathcal{L} = \sum_i \left(-\frac{1}{2}\log(2\pi\sigma^2) - \frac{1}{2}\left(\frac{T_D(\nu_i) - T_{fg}(\nu_i) - T_{21}(\nu_i)}{\sigma} \right)^2 \right), \quad (2)$$

where the temperatures T_D is the SARAS 3 data, T_{21} is the global 21-cm signal model and T_{fg} is the foreground model. In practice, the noise in a global 21-cm experiment is expected to be larger at low frequencies and decrease with increasing frequencies, following the general trend of the sky temperature. A full treatment of any frequency dependence in the noise is left for future work. However, we found (Fig. 2) that the posterior probability for σ on the assumed Gaussian noise is uncorrelated with the astrophysical parameters, and we would therefore expect a full treatment of the noise to have little impact on the derived parameter constraints for the two excess background models. We expect a full treatment of the noise to be more important in future experiments that provide tighter constraints on the astrophysical process during cosmic dawn.

Foreground modelling

The foreground model used here was identical to the one employed in the original SARAS 3 analysis[35]. The log–log polynomial foreground model is given by

$$\log_{10} T_{fg} = \sum_{i=0}^{i=6} a_i (\mathcal{R}(\log_{10}\nu))^i, \quad (3)$$

where a_i are the fitted coefficients, $\mathcal{R}$ is a normalizing function that scales its argument, $\log_{10}\nu$, linearly between −1 and +1, and ν is the frequency in megahertz. When fitting the model with POLYCHORD, we provided a uniform prior, our initial assumption about the model parameters, of −10 to +10 on each of the foreground model coefficients, a_i. In addition to the foregrounds, the model was designed to account for any residual systematics from the calibration process.

Signal modelling and emulation

At the high redshifts of cosmic dawn the most important factors that drive the 21-cm signal are the intensity of the Lyα background, which determines the efficiency of the coupling between T_S and T_K, T_{rad} and the thermal history of the gas. The dependence of the 21-cm signal on these processes is as follows: (1) the earlier star formation starts, the lower the frequency of the absorption profile will be; (2) the stronger the Lyα background, the steeper and deeper the resulting 21-cm signal will be; (3) the colder the gas, relative to the background radiation, the deeper the absorption feature will be. The resulting 21-cm signal can be written as

$$T_{21} = \frac{T_S - T_{rad}}{1+z}\left[1 - \exp(-\tau_{21})\right] \propto 1 - \frac{T_{rad}}{T_S}, \quad (4)$$

where we assumed that the Universe is largely neutral at the high redshifts of cosmic dawn.

One potential source of radio photons at cosmic dawn are early radio galaxies[44]. The radio background contribution created by such sources is proportional to the SFR, thus increasing with time, and is non-uniform following the distribution of galaxies. The radio luminosity spectrum as a function of ν produced by a star-forming region and calculated per SFR (in units of W Hz^{-1}) is given by

$$L_{\rm r} = f_{\rm radio} 10^{22} \left(\frac{\nu}{150\,{\rm MHz}}\right)^{-\alpha_{\rm radio}} \frac{\rm SFR}{M_\odot\,{\rm yr}^{-1}}, \quad (5)$$

where $f_{\rm radio}$ measures radio photon production in high-redshift galaxies compared with their present-day counterparts and $\alpha_{\rm radio} = 0.7$ is the spectral index in the radio band[45]. The temperature of the radio background produced by such galaxies at a given z was calculated by integrating over the contribution of all galaxies within the past light-cone[45] and was added to the temperature of the CMB to give the total radio background temperature. We provide constraints on the radio luminosity per SFR, $L_{\rm r}$/SFR, at a reference frequency of 150 MHz in the Results.

We took several heating and cooling mechanisms into account, such as cooling due to the expansion of the Universe and heating due to structure formation, Lyα[5,68] and CMB[69] heating, as well as heating by the first X-ray binaries[53]. In our model, the first four effects were fully determined by cosmology and star formation, whereas heating by X-ray binaries invoked new astrophysical processes (such as black hole binary formation and X-ray production by the high-redshift sources). Therefore, X-ray heating required independent parameterization, and we modelled $L_{\rm X}$ (ref. [70]) as

$$L_{\rm X,0.2-95\,keV} = 3 \times 10^{40} f_{\rm X} \frac{\rm SFR}{M_\odot\,{\rm yr}^{-1}} \quad (6)$$

in units of erg s^{-1} between 0.2 and 95 keV. Gas thermal history was then evaluated at every z by integrating over the contribution of all galaxies within the past light-cone to find the corresponding heating rate and then solving a differential equation to evolve the gas temperature.

Both the radio luminosity and the thermal history of the gas depend on the SFR, which is not well constrained for early galaxies. Therefore, our model also included free parameters that regulated star formation. One was f_*, which measures the fraction of collapsed gas in star-forming regions that turns into stars, and the other is the minimum mass of star-forming haloes, or, equivalently, $V_{\rm c}$ (ref. [71]). This quantity depends on the local environment of each star-forming region and is affected by factors such as the local intensity of the radiative background in the Lyman–Werner band[51,72] or the relative velocity between dark matter and gas[54,72,73].

To physically model the global 21-cm signal, we relied on neural network-based emulation with the PYTHON package GLOBALEMU[58] trained on the results of the full semi-numerical simulations of the global 21-cm signal[28,29,45,48,50,52].

For each global signal model, we had a series of testing and training signals. Table 2 shows the ranges of the parameters in each of the training and testing datasets for the different models of the global 21-cm signals used in this work. The boundaries correspond to the broadest possible ranges allowed for each of the parameters from the astrophysical principles and existing (weak) observational constraints. Outside these ranges, the emulators were unreliable, and consequently the ranges acted as the prior bounds for the nested sampling code POLYCHORD. The parameters were sampled either uniformly or log uniformly between the ranges in the training and test data, and we used appropriate prior probability distributions for each parameter when running the fits.

For all three signal emulators, we used the same neural network architecture with 4 hidden layers of 16 nodes each. The same radio galaxies and CMB-only emulators were recently used in our analysis of the SARAS 2 data[21]. We note that the network for the CMB-only radio background models has seven astrophysical inputs, whereas the radio galaxy and synchrotron radio background networks both have five. For the CMB-only model the X-ray spectral energy density was characterized by the slope of the spectrum, α, and a low energy cutoff, $E_{\rm min}$, whereas for the other two models, the X-ray spectral energy density was fixed to that of high-redshift X-ray binaries[70]. Furthermore, parameters related to reionization had very modest effects on the 21-cm signal in the SARAS 3 range. Therefore, we fixed the mean free path of ionizing photons. For the radio galaxies and radio synchrotron backgrounds, the mean free path was fixed to 40 Mpc, while in the CMB-only case, it was fixed to $R_{\rm mfp} = 30$ Mpc.

We assessed the accuracy of the neural networks in the SARAS 3 band, $z \approx 15$–25, using the r.m.s.e. when emulating the test data after training. The synchrotron radio background network had a mean r.m.s.e. when emulating 1034 test models, after training on 9,304 models, of 7.98 mK, a 95th percentile r.m.s.e. of 23.06 mK and worst r.m.s.e. of 85.65 mK. The CMB-only background network was trained on 5,137 models and tested on 570 models. In the SARAS 3 band, the mean r.m.s.e. for the test data was 0.78 mK, the 95th percentile r.m.s.e. was 2.67 mK and the worst r.m.s.e. was 13.36 mK. Finally, when trained on a data set of 4,311 models and tested on 479 models, the radio galaxy radio background neural network emulator was found to have a mean r.m.s.e. of 5.11 mK, a 95th percentile r.m.s.e. of 20.53 mK and worst r.m.s.e. of 81.70 mK in the SARAS 3 band. All of the trained networks had 95th percentile r.m.s.e. well below the r.m.s. found after modelling and subtracting the log–log polynomial foreground model from the SARAS 3 data. The numbers are summarized in Table 1.

When fitting all three signal models with the foreground, we saw no correlation between the astrophysical parameters and the foreground parameters. An example of this can be seen in the 2D posteriors, which are shown in Fig. 3, between the astrophysical and foreground parameters from the fit with the radio galaxies background model.

Marginal $\mathcal{D}$ and EDGES-like signals

To determine the volume of the EDGES-like parameter space that the SARAS 3 data ruled out, we calculated $\mathcal{D}$. To illustrate the types of signal that we were selecting by constraining our parameter space to be EDGES-like, we show the corresponding functional prior and posterior in Supplementary Information.

$\mathcal{D}$ is a measure of the information gained when contracting a prior onto a posterior. For our purposes we were interested in the EDGES-like parameter space, and as a result, we considered the foreground parameters to be nuisance parameters and needed to integrate them out.

To calculate the marginal $\mathcal{D}$, we therefore needed to evaluate the log-probabilities associated with the signal parameters in the EDGES-like prior, π, and the corresponding posterior, $\mathcal{P}$:

$$D(\mathcal{P}\|\pi) = \int \mathcal{P}(\theta) \log_{\rm e}\left(\frac{\mathcal{P}(\theta)}{\pi(\theta)}\right) {\rm d}\theta = \langle \log_{\rm e}\left(\frac{\mathcal{P}(\theta)}{\pi(\theta)}\right) \rangle_{\mathcal{P}}. \quad (7)$$

We used a Gaussian kernel density estimator to replicate the samples in the signal sub-spaces of our EDGES-like prior and posterior via the recently developed code MARGARINE[74,75]. A multivariate Gaussian kernel density estimator, implemented with SCIPY, was produced by summing over multiple multivariate Gaussian profiles with a known standard deviation centred around each sample point; the log of the probability density function was consequently easily tractable, making the KL divergence easily calculable.

When training our kernel density estimators on the prior and posterior samples, we first transformed our data into the standard normal parameter space, which improved the accuracy of the density estimator and allowed it to better capture the sharp edges of approximately flat distributions.

It can be shown that $\mathcal{D}$ is related to the volume fraction between the posterior and the prior via:

$$\mathcal{D}(\mathcal{P}||\pi) = \log_e\left(\frac{V_{\mathcal{P}}}{V_\pi}\right), \quad (8)$$

and therefore:

$$\exp(-\mathcal{D}(\mathcal{P}||\pi)) = \frac{V_\pi}{V_{\mathcal{P}}}, \quad (9)$$

can be used to determine the volume of the prior contained in the posterior or, in our case, the volume of the EDGES-like prior that is still consistent with the SARAS 3 data after fitting.

Data availability

The SARAS 3 data are available upon reasonable request from S.S. (saurabhs@rri.res.in).

Code availability

GLOBALEMU is available at https://github.com/htjb/globalemu and MARGARINE at https://github.com/htjb/margarine. The nested sampling tool POLYCHORD is available at https://github.com/PolyChord/PolyChordLite and the nested sampling post-processing codes ANESTHETIC and FGIVENX are available at https://github.com/williamjameshandley/anesthetic and https://github.com/williamjameshandley/fgivenx, respectively. All other codes used are available upon reasonable request from the corresponding author.

References

1. Windhorst, R. A., Cohen, S. H., Jansen, R. A., Conselice, C. & Yan, H. How JWST can measure first light, reionization and galaxy assembly. *New Astron. Rev.* **50**, 113–120 (2006).
2. Nandra, K. et al. The hot and energetic Universe: a white paper presenting the science theme motivating the Athena+ mission. Preprint at https://arxiv.org/abs/1306.2307 (2013).
3. The Lynx Team The Lynx mission concept study interim report. Preprint at https://arxiv.org/abs/1809.09642 (2018).
4. Mushotzky, R. AXIS: a probe class next generation high angular resolution x-ray imaging satellite. In *Space Telescopes and Instrumentation 2018: Ultraviolet to Gamma Ray* SPIE Conference Series Vol. 10699 (eds den Herder, J.-W. A. et al.) 1069929 (SPIE, 2018).
5. Madau, P., Meiksin, A. & Rees, M. J. 21 centimeter tomography of the intergalactic medium at high redshift. *Astrophys. J.* **475**, 429–444 (1997).
6. Mesinger, A. (ed.) *The Cosmic 21-cm Revolution* (IOP Publishing, 2019).
7. Monsalve, R. A., Rogers, A. E. E., Bowman, J. D. & Mozdzen, T. J. Calibration of the EDGES high-band receiver to observe the global 21 cm signature from the epoch of reionization. *Astrophys. J.* **835**, 49 (2017).
8. Singh, S. et al. SARAS 2: a spectral radiometer for probing cosmic dawn and the epoch of reionization through detection of the global 21-cm signal. *Exp. Astron.* **45**, 269–314 (2018).
9. DeBoer, D. R. et al. Hydrogen Epoch of Reionization Array (HERA). *Publ. Astron. Soc. Pac.* **129**, 045001 (2017).
10. Koopmans, L. V. E. Current status of the LOFAR EoR Key Science Project. *Proc. IAU* **12**, 71–76 (2017).
11. Price, D. C. et al. Design and characterization of the Large-aperture Experiment to Detect the Dark Age (LEDA) radiometer systems. *Mon. Not. R. Astron. Soc.* **478**, 4193–4213 (2018).
12. Trott, C. M. et al. Deep multiredshift limits on epoch of reionization 21 cm power spectra from four seasons of Murchison Widefield Array observations. *Mon. Not. R. Astron. Soc* **493**, 4711–4727 (2020).
13. Gehlot, B. K. et al. The first power spectrum limit on the 21-cm signal of neutral hydrogen during the cosmic dawn at $z = 20–25$ from LOFAR. *Mon. Not. R. Astron. Soc.* **488**, 4271–4287 (2019).
14. Singh, S. et al. First results on the epoch of reionization from first light with SARAS 2. *Astrophys. J. Lett.* **845**, L12 (2017).
15. Singh, S. et al. SARAS 2 constraints on global 21 cm signals from the epoch of reionization. *Astrophys. J.* **858**, 54 (2018).
16. Monsalve, R. A. et al. Results from EDGES high-band. III. New constraints on parameters of the early Universe. *Astrophys. J.* **875**, 67 (2019).
17. Mondal, R. et al. Tight constraints on the excess radio background at $z = 9.1$ from LOFAR. *Mon. Not. R. Astron. Soc.* **498**, 4178–4191 (2020).
18. Ghara, R., Giri, S. K., Ciardi, B., Mellema, G. & Zaroubi, S. Constraining the state of the intergalactic medium during the epoch of reionization using MWA 21-cm signal observations. *Mon. Not. R. Astron. Soc.* https://doi.org/10.1093/mnras/stab776 (2021).
19. Greig, B. et al. Interpreting LOFAR 21-cm signal upper limits at $z \approx 9.1$ in the context of high-z galaxy and reionization observations. *Mon. Not. R. Astron. Soc.* **501**, 1–13 (2020).
20. Abdurashidova, Z. et al. HERA Phase I limits on the cosmic 21-cm signal: constraints on astrophysics and cosmology during the epoch of reionization. *Astrophys. J.* **924**, 51 (2022).
21. Bevins, H. T. J. et al. A comprehensive Bayesian reanalysis of the SARAS2 data from the epoch of reionization. *Mon. Not. R. Astron. Soc.* **513**, 4507–4526 (2022).
22. Mesinger, A. Was reionization complete by $z \sim 5–6$? *Mon. Not. R. Astron. Soc.* **407**, 1328–1337 (2010).
23. Schroeder, J., Mesinger, A. & Haiman, Z. Evidence of Gunn–Peterson damping wings in high-z quasar spectra: strengthening the case for incomplete reionization at $z \sim 6–7$. *Mon. Not. R. Astron. Soc.* **428**, 3058–3071 (2012).
24. Ouchi, M. et al. Systematic identification of LAEs for visible exploration and reionization research using Subaru HSC (SILVERRUSH). I. Program strategy and clustering properties of ~2000 Lyα emitters at $z = 6$-7 over the 0.3-0.5 Gpc^2 survey area. *Publ. Astron. Soc. Jpn* **70**, S13 (2018).
25. Morales, A. M. et al. The evolution of the lyman-alpha luminosity function during reionization. *Astrophys. J.* **919**, 120 (2021).
26. Greig, B. et al. IGM damping wing constraints on reionization from covariance reconstruction of two $z \gtrsim 7$ QSOs. *Mon. Not. R. Astron. Soc.* **512**, 5390–5403 (2022).
27. Bowman, J. D., Rogers, A. E. E., Monsalve, R. A., Mozdzen, T. J. & Mahesh, N. An absorption profile centred at 78 megahertz in the sky-averaged spectrum. *Nature* **555**, 67–70 (2018).
28. Cohen, A., Fialkov, A., Barkana, R. & Lotem, M. Charting the parameter space of the global 21-cm signal. *Mon. Not. R. Astron. Soc.* **472**, 1915–1931 (2017).
29. Reis, I., Fialkov, A. & Barkana, R. The subtlety of Ly α photons: changing the expected range of the 21-cm signal. *Mon. Not. R. Astron. Soc.* **506**, 5479–5493 (2021).
30. Feng, C. & Holder, G. Enhanced global signal of neutral hydrogen due to excess radiation at cosmic dawn. *Astrophys. J. Lett.* **858**, L17 (2018).
31. Barkana, R. Possible interaction between baryons and dark-matter particles revealed by the first stars. *Nature* **555**, 71–74 (2018).
32. Girish, B. S. et al. SARAS CD/EoR radiometer: design and performance of the digital correlation spectrometer. *J. Astron. Instrum.* **9**, 2050006–70 (2020).

33. Raghunathan, A. et al. A floating octave bandwidth cone-disc antenna for detection of cosmic dawn. *IEEE Trans. Antennas Propag.* **69**, 6209–6217 (2021).
34. Nambissan T., J. et al. SARAS 3 CD/EoR radiometer: design and performance of the receiver. *Exp. Astron.* https://doi.org/10.1007/s10686-020-09697-2 (2021).
35. Singh, S. et al. On the detection of a cosmic dawn signal in the radio background. *Nat. Astron.* **6**, 607–617 (2022).
36. Hills, R., Kulkarni, G., Meerburg, P. D. & Puchwein, E. Concerns about modelling of the EDGES data. *Nature* **564**, E32–E34 (2018).
37. Singh, S. & Subrahmanyan, R. The redshifted 21 cm signal in the EDGES low-band spectrum. *Astrophys. J.* **880**, 26 (2019).
38. Bradley, R. F., Tauscher, K., Rapetti, D. & Burns, J. O. A ground plane artifact that induces an absorption profile in averaged spectra from global 21 cm measurements, with possible application to EDGES. *Astrophys. J.* **874**, 153 (2019).
39. Sims, P. H. & Pober, J. C. Testing for calibration systematics in the EDGES low-band data using Bayesian model selection. *Mon. Not. R. Astron. Soc.* **492**, 22–38 (2020).
40. Mellema, G. et al. Reionization and the cosmic dawn with the Square Kilometre Array. *Exp. Astron.* **36**, 235–318 (2013).
41. Zarka, P. et al. The low-frequency radiotelescope NenuFAR. In *2018 2nd URSI Atlantic Radio Science Meeting (AT-RASC)* 1 (IEEE, 2018).
42. Gehlot, B. K. et al. The AARTFAAC Cosmic Explorer: observations of the 21-cm power spectrum in the EDGES absorption trough. *Mon. Not. R. Astron. Soc.* **499**, 4158–4173 (2020).
43. de Lera Acedo, E. REACH: Radio experiment for the analysis of cosmic hydrogen. In *2019 International Conference on Electromagnetics in Advanced Applications* 0626 (IEEE, 2019).
44. Mirocha, J. & Furlanetto, S. R. What does the first highly redshifted 21-cm detection tell us about early galaxies? *Mon. Not. R. Astron. Soc.* **483**, 1980–1992 (2019).
45. Reis, I., Fialkov, A. & Barkana, R. High-redshift radio galaxies: a potential new source of 21-cm fluctuations. *Mon. Not. R. Astron. Soc.* **499**, 5993–6008 (2020).
46. Ewall-Wice, A. et al. Modeling the radio background from the first black holes at cosmic dawn: implications for the 21 cm absorption amplitude. *Astrophys. J.* **868**, 63 (2018).
47. Jana, R., Nath, B. B. & Biermann, P. L. Radio background and IGM heating due to Pop III supernova explosions. *Mon. Not. R. Astron. Soc.* **483**, 5329–5333 (2019).
48. Fialkov, A. & Barkana, R. Signature of excess radio background in the 21-cm global signal and power spectrum. *Mon. Not. R. Astron. Soc.* **486**, 1763–1773 (2019).
49. Mirocha, J. ARES: accelerated reionization era simulations. *Astrophysics Source Code Library* ascl:2011.010 (2020).
50. Visbal, E., Barkana, R., Fialkov, A., Tseliakhovich, D. & Hirata, C. M. The signature of the first stars in atomic hydrogen at redshift 20. *Nature* **487**, 70–73 (2012).
51. Fialkov, A., Barkana, R., Visbal, E., Tseliakhovich, D. & Hirata, C. M. The 21-cm signature of the first stars during the Lyman-Werner feedback era. *Mon. Not. R. Astron. Soc.* **432**, 2909–2916 (2013).
52. Fialkov, A. & Barkana, R. The rich complexity of 21-cm fluctuations produced by the first stars. *Mon. Not. R. Astron. Soc.* **445**, 213–224 (2014).
53. Fialkov, A., Barkana, R. & Visbal, E. The observable signature of late heating of the Universe during cosmic reionization. *Nature* **506**, 197–199 (2014).
54. Fialkov, A., Barkana, R., Tseliakhovich, D. & Hirata, C. M. Impact of the relative motion between the dark matter and baryons on the first stars: semi-analytical modelling. *Mon. Not. R. Astron. Soc.* **424**, 1335–1345 (2012).
55. Klessen, R. in *Formation of the First Black Holes* (eds Latif, M. & Schleicher, D.) Ch. 4 (World Scientific, 2019).
56. Wouthuysen, S. A. On the excitation mechanism of the 21-cm (radio-frequency) interstellar hydrogen emission line. *Astron. J.* **57**, 31–32 (1952).
57. Field, G. B. The spin temperature of intergalactic neutral hydrogen. *Astrophys. J.* **129**, 536 (1959).
58. Bevins, H. T. J., Handley, W. J., Fialkov, A., de Lera Acedo, E. & Javid, K. GLOBALEMU: a novel and robust approach for emulating the sky-averaged 21-cm signal from the cosmic dawn and epoch of reionization. *Mon. Not. R. Astron. Soc.* **508**, 2923–2936 (2021).
59. Skilling, J. Nested sampling. *AIP Conf. Proc.* **735**, 395–405 (2004).
60. Kullback, S. & Leibler, R. A. On information and sufficiency. *Ann. Math. Stat.* **22**, 79–86 (1951).
61. Fixsen, D. J. et al. ARCADE 2 measurement of the absolute sky brightness at 3-90 GHz. *Astrophys. J.* **734**, 5 (2011).
62. Dowell, J. & Taylor, G. B. The radio background below 100 MHz. *Astrophys. J.* **858**, L9 (2018).
63. Subrahmanyan, R. & Cowsik, R. Is there an unaccounted for excess in the extragalactic cosmic radio background? *Astrophys. J.* **776**, 42 (2013).
64. Anstey, D., de Lera Acedo, E. & Handley, W. A general Bayesian framework for foreground modelling and chromaticity correction for global 21 cm experiments. *Mon. Not. R. Astron. Soc.* **506**, 2041–2058 (2021).
65. de Lera Acedo, E. et al. The REACH radiometer for detecting the 21-cm hydrogen signal from redshift $z \approx 7.5$–28. *Nat. Astron.* **6**, 984–998 (2022).
66. Handley, W. J., Hobson, M. P. & Lasenby, A. N. POLYCHORD: nested sampling for cosmology. *Mon. Not. R. Astron. Soc.* **450**, L61–L65 (2015).
67. Handley, W. J., Hobson, M. P. & Lasenby, A. N. POLYCHORD: next-generation nested sampling. *Mon. Not. R. Astron. Soc.* **453**, 4385–4399 (2015).
68. Chuzhoy, L. & Shapiro, P. R. Heating and cooling of the early intergalactic medium by resonance photons. *Astrophys. J.* **655**, 843–846 (2007).
69. Venumadhav, T., Dai, L., Kaurov, A. & Zaldarriaga, M. Heating of the intergalactic medium by the cosmic microwave background during cosmic dawn. *Phys. Rev. D* **98**, 103513 (2018).
70. Fragos, T., Lehmer, B. D., Naoz, S., Zezas, A. & Basu-Zych, A. Energy feedback from X-ray binaries in the early Universe. *Astrophys. J.* **776**, L31 (2013).
71. Barkana, R. & Loeb, A. In the beginning: the first sources of light and the reionization of the Universe. *Phys. Rep.* **349**, 125–238 (2001).
72. Schauer, A. T. P., Glover, S. C. O., Klessen, R. S. & Clark, P. The influence of streaming velocities and Lyman–Werner radiation on the formation of the first stars. *Mon. Not. R. Astron. Soc.* **507**, 1775–1787 (2021).
73. Tseliakhovich, D. & Hirata, C. Relative velocity of dark matter and baryonic fluids and the formation of the first structures. *Phys. Rev. D* **82**, 083520 (2010).
74. Bevins, H. T. J. et al. Removing the fat from your posterior samples with margarine. Preprint at https://arxiv.org/abs/2205.12841 (2022).
75. Bevins, H. et al. Marginal Bayesian statistics using masked autoregressive flows and kernel density estimators with examples in cosmology. *Phys. Sci. Forum* **5**, 1 (2022).
76. Handley, W. anesthetic: nested sampling visualisation. *J. Open Source Softw.* **4**, 1414 (2019).
77. Handley, W. fgivenx: a Python package for functional posterior plotting. *J. Open Source Softw.* **3**, 849 (2018).

Acknowledgements

H.T.J.B. acknowledges the support of the Science and Technology Facilities Council (STFC) through grant number ST/T505997/1. W.J.H. and A.F. were supported by Royal Society University Research

Fellowships. E.d.L.A. was supported by the STFC through the Ernest Rutherford Fellowship. R.B. acknowledges the support of the Israel Science Foundation (grant number 2359/20), The Ambrose Monell Foundation and the Institute for Advanced Study, as well as the Vera Rubin Presidential Chair in Astronomy and the Packard Foundation.

Author contributions

H.T.J.B. performed the data analysis and led the writing of the paper. A.F. initiated the project, supervised it and helped write and revise the article. E.d.L.A. supervised the project and the analysis and helped write and revise the article. W.J.H. provided technical support and advice regarding the Bayesian methodology. R.S. and S.S. provided the non-public data used in the analysis. The astrophysical signal models were provided by A.F. and R.B. All authors provided comments and contributed to the structure of the article.

Competing interests

The authors declare no competing interests.

Additional information

Supplementary information The online version contains supplementary material available at https://doi.org/10.1038/s41550-022-01825-6.

Correspondence and requests for materials should be addressed to H. T. J. Bevins.

Peer review information *Nature Astronomy* thanks the anonymous reviewers for their contribution to the peer review of this work.